Ingeniería y Ciencia, ISSN 1794–9165
Volumen 4, número 8, diciembre de 2008, páginas 65–84

CFD Analysis of the Effect on Buoyancy Due to Terrain Temperature Based on an Integrated DEM and Landsat Infrared Imagery

Análisis CFD de vientos convectivos naturales debidos a la temperatura de un terreno basado en un modelo DEM integrado con imágenes infrarrojas Landsat

Manuel García[1], Pierre Boulanger[2], Juan Duque[3] and Santiago Giraldo[4]

Recepción: 24-abr-2008/Modificación: 28-oct-2008/Aceptación: 28-oct-2008
Se aceptan comentarios y/o discusiones al artículo

Abstract
This paper deals with the influence of concrete structures on atmospheric temperature and the convection winds generated in the Aburra Valley in Medellín, Colombia. This area is characterised by low wind velocities with a high industry density. A digital elevation model was used from the Radar Shuttle Topography Mission and post-processed in order to obtain a valid volumetric CFD domain. The construction process includes hole-filling due to imperfections in the original radar data, decimation of the original cloud-of-points to

[1] PhD in Aeronautical Engineering, mgarcia@eafit.edu.co, Associate professor, Applied Mechanics Research Group, Mechanical engineering Department, EAFIT University, Medellín–Colombia.
[2] PhD in Physics, pierreb@cs.ualberta.ca, Associate professor, Director AMMI Lab, University of Alberta, Edmonton–Canada.
[3] Mech Eng., jduquelo@eafit.edu.co, Research assistant, Applied Mechanics Research Group, Mechanical Engineering Department, EAFIT University, Medellín–Colombia.
[4] Mech Eng., sgiral6@eafit.edu.co, Research assistant, Applied Mechanics Research Group, Mechanical Engineering Department, EAFIT University, Medellín–Colombia.

reduce the excess of detail in regions with low curvature, and the introduction of a volume of air over the terrain surface (CFD domain). Landsat satellite data was used to set the terrain temperatures for various material compositions. The converted infrared image was then registered into the CFD domain using an interpolation technique.

Navier–Stokes Equations were solved for buoyant, turbulent flow of compressible fluids accounting for convection and heat transfer effects. Simulation includes buoyancy and turbulence flow through the k–epsilon model using the high-performance computing facilities of Westgrid (Western Canada Research Grid). Preliminary results show wind distributions that compare to the one observed at low–altitude in the region.

Key words: Buoyancy, Landsat, Digital Elevation Models, Computational Fluid Dynamics.

Resumen

El presente trabajo estudia la influencia de estructuras de concreto en la temperatura atmosférica y los vientos convectivos generados en el Valle de Aburrá en Medellín, Colombia. Esta zona se caracteriza por vientos de bajas velocidades con alta densidad industrial. Un modelo de elevación digital fue obtenido de la misión topográfica del radar Shuttle y post-procesado en aras de obtener un dominio volumétrico CFD válido. El proceso de construccion incluye el parchado de agujeros debidos a imperfectos en los datos originarios del radar, decimación de la nube de puntos original para reducir el exceso de detalle en regiones con baja curvatura y la generación de un volumen de aire sobre la superficie del terreno (Dominio CFD). Datos obtenidos de la misión satelital Landsat fueron utilizados para establecer temperaturas sobre el terreno para distintos materiales y fue mapeada sobre el terreno utilizando técnicas de interpolación.

Las ecuaciones de Navier–Stokes fueron solucionadas para modelos de fenómenos de convección natural con efectos de flujo turbulento de fluidos compresibles, tomando en cuenta efectos convectivos y de transferencia de calor. La simulación incluye convección y condiciones de turbulencia bajo el modelo k–epsilon utilizando las instalaciones de computación de alto desempeño de Westgrid (Western Canada Research Grid). Los resultados preliminares muestran distribuciones de viento comparables a las observadas en la región de baja altitud.

Palabras claves: convección natural, Landsat, digital elevation models, dinámica de fluidos computacional.

1 Introduction

Wind standards and codes–of–practice typically assume a terrain of homogeneous roughness or provide explicit corrections for specific topographies such as hills or escarpments. For more complex situations they refer the practitioner to boundary layer wind tunnel tests. With the fast evolution of computers and algorithms, numerical low altitude wind simulation has become very attractive as it provides a low–cost alternative to evaluate wind effects.

This paper presents and discusses a methodology for numerical evaluation of buoyancy effects over complex terrain topographies. Computational domain is obtained by using digital elevation models which allow automatic reconstruction of any terrain surface on earth. Solution is obtained by solving the Navier–Stokes equations using the OpenFOAM (Open Source Field Operation and Manipulation) toolkit using the high performance computing facilities of Westgrid[1].

This application is particularly useful for mountainous regions with reduced wind speed due to mountain protection. Applications include atmospheric heating and dispersion of pollutants in these areas. This model could help predict how contaminants disperse and reach populated areas. CFD simulation could provide a way to relocate factories near cities to minimise pollution effects [1, 2, 3, 4].

Digital elevation models have been used by P. W. Cleary and M. Prakash [5] to simulate several geophysical situations. They use the Smooth Particle Hydrodynamic Method to simulate the failure of a dam. The waves generated by a Tsunami and volcano lava flows. They also used Discrete–element modelling to simulate landslides. Wang et al [6] use the Finite Element Method and a Lagrangian particle technique to simulate contaminant transport for emergency response. The CFD domain is created using digital elevation data. Finally a combination of digital elevation data and Landsat satellite images is used by Hansen et al [7] to estimate the net short–wave radiation over a terrain surface.

[1] Western Canada Research Grid

2 Digital Elevation Models

Digital Elevation Models (DEM) are a representation of elevation data of the earth's surface. They are organised in several files which contain latitude, longitude, and elevation coordinates of points over the earth's surface. One of the most complete collections of high–resolution DEM was acquired by the Shuttle Radar Topography Mission (SRTM) [8]. Measurements were collected during a single eleven–day Endeavor Space Shuttle mission, STS–99, in February 2000 using a synthetic aperture radar. Topographic data was collected for dry land only, between 56 degrees south latitude and 60 degrees north latitude, covering a total of about eighty per cent of the Earth's surface.

The data gathered during the mission was processed and organised in two ways: a) Square segments covering one degree latitude by one degree longitude. Every segment was saved in a distinct file. Every file is organised as a grid of n rows and m columns of samples whose distance is either one arc second (1/3600 of degree) for the United States (SRMT) or three arc seconds (SRMT3) for the rest of the world. b) Processed data can also be retrieved through the Seamless Data Distribution System (SDDS) of the US Geological Survey (USGS) and the EROS Data Center (EDC) service (2003). The main feature is that the user can define an area of interest by drawing a box, defining coordinates, or using available templates to cut a particular area of interest. They also offer a variety of DEM formats. One arc second measured at the equator corresponds approximately to thirty meters, so two sampling points in a STRM3 file are roughly ninety meters from each other. This approximation will deteriorate as one moves away from the equator in the direction of either pole.

Every sample is represented with a sixteen–bit signed integer, row–ordered. Integer coding is *big endian*, meaning that the first byte read is the most significant and the second is the least significant. The number associated with each sample corresponds to its elevation measured in meters with respect to the WGS84 EGM96 geoid. (A geoid is a rotational solid used in geodesy that approximates the shape of the Earth better than a sphere or an ellipsoid.) Data files are not perfect and some *voids* are present. They are created by shadow or water reflections which create distortions. Samples corresponding to these voids are given a conventional value of -32768 in the NASA files and 0 in the SDDS files.

3 Digital Terrain Thermal Distribution Using Landsat Infrared Imagery

The observation of the Earth by the Landsat satellite and the imagery obtained from such missions goes back more than three decades to 1972. Through MSS and Thematic Mapper (TM), image data has been acquired to set an unprecedented record of the Earth's surface coverage within spatial scales of 30 and 80 m. TM sensors were included in Landsat Missions 4 (1982 – 1993) and 5 (1984 – present), but MSS sensors have been on board from Missions 1 through 5.

The global coverage obtained by the US of MSS and TM data has only been interrupted during the failure of the Ku–band transmitter, which led to loss of access to the Tracking and Data Relay Satellite System. By using data from international ground stations some of this gaps have been filled. The US began acquiring data once again with the launch of Landsat–7 Enhanced Thematic Mapper Plus (ETM+) in 1999, which included solid–state recorders. On April 15 of 1999, the satellite mission Landsat–7 was launched with the objective of acquiring well–calibrated data about the current status of the Earth's landscapes [9].

The Enhanced Thematic Mapper Plus (ETM+) used during this mission provides results of 30–meter spaced data in six consecutive spectral bands (named respectively the $1^{st}, 2^{nd}, 3^{rd}, 4^{th}, 5^{th}$, and 7^{th} band), 15–meter data in one panchromatic band (named PAN 8th band) and finally, one thermal band (6th Band). See table 1 for the respective wavelengths and the number of sensors associated with each band [10].

All data obtained on each band is acquired in one or two gain states of the instrument and mapped onto an eight bit code. For more information regarding the Landsat missions and instruments, see [10]. Top of Atmosphere (TOA) radiance is measured with the Thermal Infra–Red (TIR) sensors of the satellite. The radiance is transformed into brightness temperature (or black–body temperature) using Planck's law [11]. The combination of the emitted radiance from the Earth's surface, the upward radiance from the atmosphere, and the downward radiance from the sky sum together to deliver the TOA radiance. Depending on the atmospheric conditions, land surface brightness, and TOA, temperatures differ within a 1 to 5°K range in the

Table 1: Landsat bands and wavelengths

Band	Wavelength (nm)	Spacing (m)
1^{st}	$[441 - 514]$	30
2^{nd}	$[519 - 601]$	30
3^{rd}	$[631 - 692]$	30
4^{th}	$[772 - 898]$	30
5^{th}	$[1547 - 1748]$	30
7^{th}	$[2064 - 2346]$	30
PAN (8^{th})	$[515 - 896]$	15
Thermal (6^{th})	$[10440 - 12420]$	60

$10 - 12$ μm spectral region [12]. Corrections of atmospheric effects like absorption, upward emission, and downward irradiance reflected from the surface, must be done before obtaining land surface brightness temperatures [13]. To obtain a more accurate LST, roughness properties of the land surface, the amount and nature of vegetation cover, and the thermal properties and moisture content of the soil must be accounted for by correcting brightness temperatures using spectral emissivity values before computation occurs [14].

4 Creation of a CFD Domain from DEM Data

CFD domains are created from the DEM information and should cover a large enough portion to guarantee accuracy in the simulation. For wind simulation, a volume of air over the surface constitutes the CFD domain. Data from the SRMT should be completed to generate the domain.

4.1 Void Management

Voids can be filled in different ways which include several interpolation techniques. Also, information from other sources like other DEM databases or

GPS measurements can be used to complete the data. A simple interpolation technique uses information from the closest points around a void $\vec{x}$,

$$z(\vec{x}) = \frac{1}{n} \sum_{\vec{q}_j \in \Omega_x}^{n} w_j \; z(\vec{q}_j), \;\; \Omega_x = \left\{ \vec{q}_j \;\middle|\; ||\vec{x} - \vec{q}_j|| < r \right\},$$

with w_j a weight factor and $r \in \mathbb{R}$. The disadvantage of this is that due to the nature of the holes (they can be large in one direction), it could result in a good approximation in one direction and a deficient approximation of the slope and curvature in the other direction. This weighted average can be further enhanced if a least square approximation is taken over a patch $||\vec{x} - \vec{q}|| < r$ around a void [15]. However, it is the shape of the patch that it should be considered.

Thus the following interpolation takes the weighted average of the closest points different to zero (valid points) in all directions (North, East, West, South). The weight is the inverse of the distance, and therefore the closest points have the largest weight. The weight equation is

$$z(\vec{x}) = \left(\frac{1}{\sum_j w_j} \right) \sum_{j \in \Omega} w_j z(\vec{q}_j) \,,$$

with $w_j = \frac{1}{||\vec{x} - \vec{q}_j||}$ and $\Omega_x = \vec{q}_j$ such that $\min ||\vec{x} - \vec{q}_j||$, for each $\vec{q}_j$ taken in the North, East, South, and West directions and $z(\vec{q}_j) \neq 0$.

4.2 Mesh Generation

The finished DEM data is transformed into a regular grid of triangular elements, e.g., a two–manifold with boundary that represents the terrain surface. SRMT data files cover an approximate area of 108×108 km. As SRMT3 data is sampled at every three arc sec it contains in total $1,442,401$ equidistant points. This surface can be efficiently decimated preserving the curvature detail by suppressing points at low–curvature regions. Depending on the topography of the terrain it can be reduced up to fifteen per cent or even ten per cent of the original data while keeping the approximation error low.

The CFD domain consists of a volume of air over the terrain surface. It can be generated by projecting vertical walls along the sampled terrain boundary

and then intersecting the resulting shell with a horizontal plane at a given height h. The final manifold must be closed and topologically correct (see figure 1). Once a correct superficial mesh of the domain is obtained, a volumetric mesh is generated. An ideal mesh for the volume element method consists of hexahedral elements. However, this is difficult to obtain automatically and there are several research groups working on this problem. An alternative to hexahedral meshes is the so–called unstructured tetrahedral meshes.

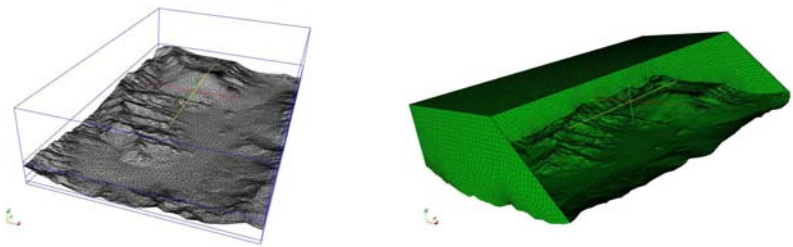

(a) Terrain surface after decimation (b) Cut of the CFD domain over the terrain surface

Figure 1: Superficial mesh and domain for CFD analysis

Unstructured tetrahedral meshes should be used with caution when implementing the volume element method and orthogonal correctors should be used to assure convergence. In this study tetrahedral meshes are generated using NETGEN [16]. The NETGEN algorithm can be summarised as follows: It starts from either a CAD model or a superficial mesh in STL format that should be topologically correct. NETGEN starts by computing the corner points and edges that are meshed into segments and the faces are meshed by an advancing front surface mesh generator. Face meshes are optimised to obtain a good quality superficial mesh. The domain is filled with tetrahedral volumetric elements using a fast Delaunay algorithm. This generates most of the elements but it often fails to complete the whole domain. Then, a slower backtracking rule–based algorithm takes over and completes the task. As a final step the volumetric mesh is optimised by the standard node–movement, element swapping, and splitting algorithms [16].

Mesh–grading towards the terrain is not necessary when using the standard $k - \epsilon$ model with wall functions since the flow in the near wall cell is modelled, rather than having to be resolved. Nevertheless, due to the size of the domain, a moderate grading is maintained in order to reduce the mesh size.

5 Boundary Conditions

Due to the boxed shape of the domain, boundary surfaces are: the terrain surface, the south, north, east and west walls, and the top surface. The main goal was to simulate wind by buoyancy effects due to heating of the terrain by solar radiation.

5.1 Conversion of Landsat Data into Surface Temperature

Two approaches to recover Land Surface Temperature (LST) from multi–spectral TIR imagery have been developed. One corrects the at–sensor radiance to surface radiance using a radiative transfer equation; later temperature and emissivity are obtained from surface radiance applying an emissivity model [17]. The other approach uses a split–window technique for sea surfaces to land surfaces and assumes that emissivity in the channels used for the split window is similar [11]. Then with a linear combination of the two channels' surface brightness temperatures are calculated. The most noticeable disadvantage of this method is that the coefficients are only valid for the data sets from which they were derived [11]. This means that extrapolation of a set of thermal responses for a process or a specific landscape phenomenon measured using a specific TIR sensor is not possible and TIR measurements from other sensors or from images recorded at different times using this same sensor cannot be predicted.

5.2 Derivation of Land Surface Temperature from Landsat ETM+ imagery

Using the corrected ETM+ TIR band (10440–12420 nm) LST were derived. To convert the Digital Number (DN) ranging from 0–255 of the Landsat

ETM+TIR band into spectral radiance, the following equation was used [10]:

$$L_\lambda = 0.0370588\ DN + 3.2\,.$$

Assuming uniform emissivity, the satellite brightness temperature (Black–body Temperature, T_B) can be obtained converting the spectral radiance [10]. The formula used for the conversion is

$$T_B = \frac{K_2}{\ln\left(\frac{K_1}{L_\lambda} + 1\right)}\,,$$

where T_B is effective at–satellite temperature in °K, L_k is the spectral radiance in W/(m^{2}steradian); as well, $K_2 = 1282.71$°K and $K_1 = 666.09$ mW $\cdot$ cm$^{-2}\cdot$sr$^{-1}\cdot\mu$m^{-1} are taken as pre–launch calibration constants for Landsat–7 ETM+ mission [10].

Since the temperature values obtained previously are referenced to a black body, corrections for spectral emissivity (ϵ) depending on the nature of land cover became necessary. The land surface temperatures (S_T) that already have been corrected with emissivity were computed as follows [18]

$$S_T = \frac{T_B}{1 + \left(\lambda\ \frac{T_B}{\rho}\right)\ln\varepsilon}\,, \tag{1}$$

where: λ is the wavelength of the emitted radiance (taking for this case a value of (λ =11500 nm) as the peak response and the average of the limiting wavelengths), β = Boltzmann constant ($1.38\cdot10^{-23}$J/K), $\rho = h\cdot c/\beta$ = ($1.438\cdot10^{-2}$ m°K), h = Planck's constant ($6.626\cdot10^{-34}$ Js), and c = velocity of light ($2.998\cdot10^{8}$ m/s).

Using the near–infrared (0.76–0.90 μm) and visible (0.63–0.69μm) bands of the ETM+ image the Normalised Difference Vegetation Index (NDVI) can be computed, bringing forth a new possible set of studies for the relationship between LST and NDVI. From equation 2 the index can be calculated, the information from the third and fourth bands of Landsat data are needed for such calculation.

$$\text{NDVI} = \frac{(\text{B4}_{i,j} - \text{B3}_{i,j})}{(\text{B4}_{i,j} + \text{B3}_{i,j})}\,, \tag{2}$$

where: $B4_{i,j}$ is the value of the i, j pixel in the fourth band dataset, and B3 is the value of the correspondent i, j pixel in the third band dataset.

A relation between emissivity and the NDVI index is possible when the NDVI value ranges between 0.157 and 0.727 [19], such relation is expressed in the following equation derived by Zhang et al (see [20]).

$$\varepsilon = 1.0094 + 0.047 \ln(\text{NDVI}) .$$

For values outside these bounds an arbitrary value can be set according to typical land cover depending on the terrain to analyse. Vegetation, bare ground, plant species and soil type, as well as pixel resolution can generate a variation on the NDVI index [21].

With the emissivity calculated for each node of the surface, a corrected land surface temperature with variable emissivity is obtained from Eq. 1 and then mapped to the mesh. From equation 1 the following expressions can be derived:

$$0 = 1 + \left(\frac{\lambda T_B}{\rho}\right) \ln\varepsilon \tag{3}$$

$$T_B = \frac{-\rho}{\lambda \ln\varepsilon} . \tag{4}$$

The model used to map effective at–satellite temperatures T_B in the Surface temperature S_T domain (Equation 1) fails for values close to the ones derived from the condition presented on the Equations 3 and 4 (All the T_B in function ε that cannot be mapped to the S_T set). Figure 2 displays the complete set of physically un–mappable T_B for emissivities ranging on the interval [0,0.9]. As the emissivity of the body in question gets closer to the one of perfect black body ($\varepsilon = 1$), the un–mappable temperature values grow exponentially to temperatures physically impossible under earth's current conditions, allowing the model portrayed by Equation 1 to properly work under a larger range of valid temperatures.

For this simulation, an interpolated value of emissivities was used across the whole terrain. The range of at–satellite temperatures was checked and proved to be physically suitable for the surface temperature mapping (Equation 1) over the terrain. Figure 3 displays the range of surface temperature values (contained between the two curves) possibly mapped over the terrain surface.

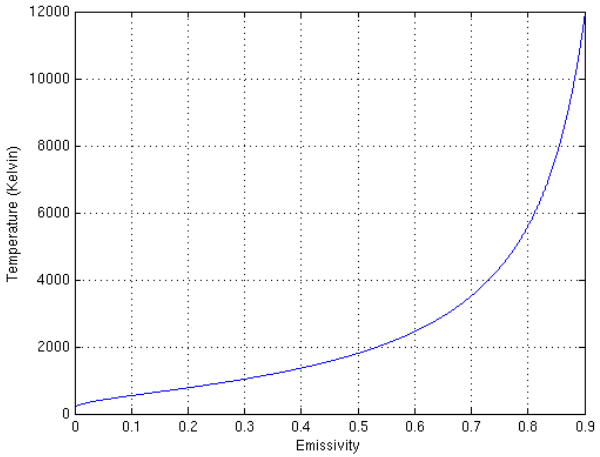

Figure 2: Un–mappable T_B values for emissivities between $[0 - 0.9]$

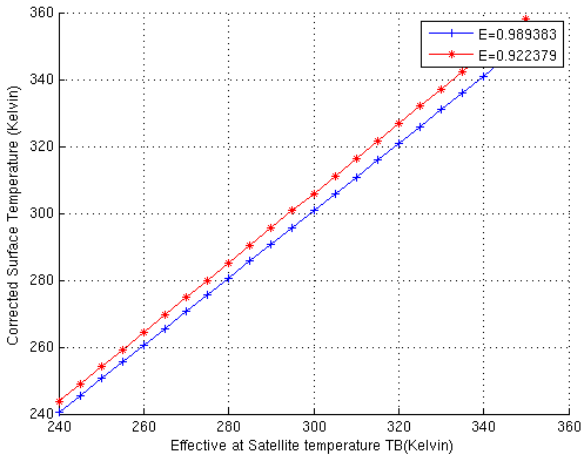

Figure 3: Mapping of effective at satellite temperatures ($T_B@\{0.922379, 0.9\}\varepsilon$)

5.2.1 Other Boundary Conditions. The initial conditions for the inside of the CFD domain are:

- *Velocity:* Uniform initial velocity of $\vec{u} = (0, 0, 0)$ m/s.
- *Temperature:* Uniform initial temperature of 242°K (see [22] for the model).
- *Pressure:* Uniform initial pressure of 1 atm.

For the boundaries of the CFD domain the boundary conditions were set as follows:

- *Terrain:* No–slip wall conditions, Variable temperature mapping over the terrain, fixed flux buoyant pressure.
- *Top Surface:* No–slip wall conditions, Constant temperature mapping of 242°K, fixed flux buoyant pressure.
- *North, South, East, West:* No–slip wall conditions, Zero gradient of temperature condition, fixed flux buoyant pressure.

6 Buoyancy Model

Buoyancy effects is simulated using the OpenFoam toolkit. OpenFOAM is the Open Source Field Operation and Manipulation (OpenFOAM) C++ library used primarily to create applications [23, 24].

The governing equations are the mass continuity equation

$$\frac{\partial \rho}{\partial t} + \nabla \cdot (\rho \vec{U}) = 0\,.$$

And the Momentum equation

$$\frac{\partial \rho \vec{U}}{\partial t} + \nabla \cdot (\rho \vec{U} \cdot \vec{U}) - \nabla \cdot \mu_{eff}(\nabla \vec{U} + \nabla \vec{U}^T) - \frac{2}{3}\mu_{eff}(\nabla \cdot \vec{U}) = -\nabla p_d - \nabla \rho \vec{g} h\,,$$

where $\mu_{eff} = \mu_{laminar} + \mu_{turbulent}$ for which $\mu_{laminar}$ is the laminar kinematic viscosity and $\mu_{turbulent}$ is the turbulent viscosity, $\rho\vec{g}$ is the buoyancy term and ρ is the reference density.

The pressure correction equation

$$\frac{\partial \psi p_d}{\partial t} + \frac{\partial \psi}{\partial t} \cdot p_{ref} + \frac{\partial \psi \rho}{\partial t} + \nabla(\rho \vec{U}) - \triangle(\rho \vec{U}) \cdot p_d \,,$$

where $\psi = \frac{1}{RT}(\mathrm{s}^2/\mathrm{m}^2)$ – compressibility, being R the gas constant.

The energy equation

$$\frac{\partial(\rho h)}{\partial t} + \nabla \cdot (\rho \vec{U}) - \nabla \cdot (\alpha_{eff} \nabla h) = \frac{\partial p}{\partial t} + \vec{U} \cdot \nabla p \,,$$

where α_{eff} is the thermal diffusivity (for enthalpy) and is given by $\alpha_{eff} = \alpha_{laminar} + \alpha_{turbulent}$, and the total pressure p is given by $p = p_d + \rho g h + p_{ref}$, where p_d is dynamic pressure, $\rho g h$ is static pressure, g is gravity and $p_r ef$ is reference pressure.

And the equation of state (for an ideal gas)

$$\rho = pRT \,,$$

where R is the gas constant.

7 The Aburra Valley

A rectangular subset of the Aburra Valley was analysed. The coordinates of the lower–left point of the area are 425 000 East and 678 000 North WGS84 UTM datum 18. In Geographic Coordinates it corresponds to −75° 40' 40.1448" West and 6.133347 6° 8' 0.0492" North. The size of the rectangular area is 15480 m (West–East) by 24390 m (South-North). DEM data with the same coordinates was selected from the SDDS site. The minimum height of the terrain is 1414.640 m and the maximum height is 7000 m over sea level. A volume of air with a height of 5585.360 m over the valley was taken as the CFD domain.

The temperature was computed using Landsat data using the method described previously and interpolated to fit with the terrain coordinates. A first case was computed using an emissivity of 0.8 which results in temperatures ranging from 6.2 to 24.5°C over the surface. A second case was computed using a variable emissivity computed using the NDVI index which renders

temperatures between 9.2 and 29°C over the terrain. These are typical temperature values hot day in the area. Notice that a difference of 4.5 °C is obtained for the highest temperature when variable emissivity is taken into account. In other words, when the land material is taken into account the temperature rises. This is true for example when compared concrete surfaces against green areas.

Visualisation of the stream lines shows that the air recirculation is larger than in the previous case. Figure 4 shows two different views with the temperature map over the surface with an emissivity of 0.8 and some stream lines over the hottest points. The same can be observed on figure 5 but with variable emissivity. These hottest points correspond to highly constructed areas with very low green space and a high percentage of industrial plants. The stream lines correspond to the 400 s simulation time step with an emissivity of 0.8. For the variable emissivity an 800 s simulation was computed. The maximum velocity produced after this time was 0.02 m/s. Solution time was 74.49 hours with a single processor and 14 hours with eight processors for the first case.

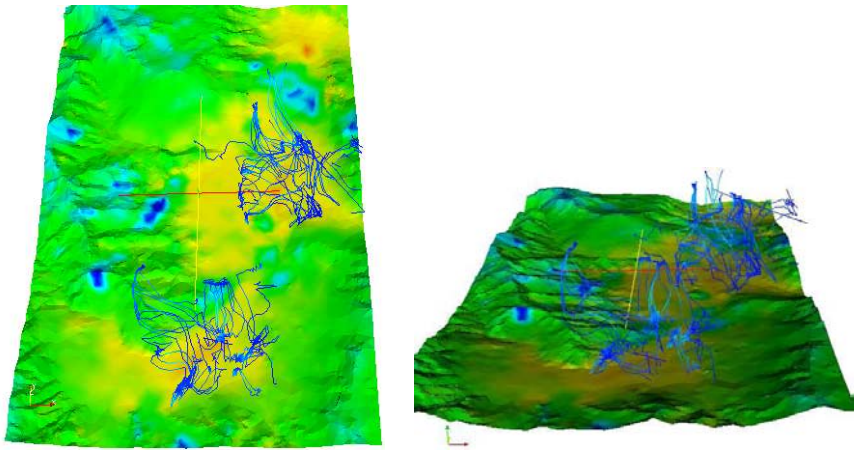

(a) Top view (b) Front-top view.

Figure 4: Terrain temperature and stream lines after 400 s. Emissivity of the terrain was taken constant at a value of 0.8

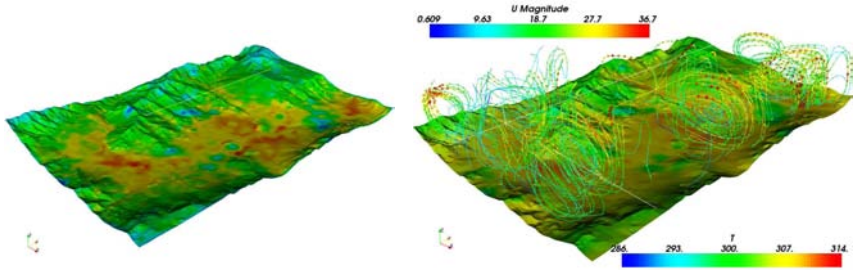

(a) Terrain (b) Terrain and streamlines

Figure 5: Terrain temperature and stream lines after 800 s. Variable emissivity corrected using NDVI

7.1 How to validate the results

The case presented here corresponds to a possible scenario of wind conditions. As it is, this simulation explores the capabilities of CFD to model complex atmospheric processes. It has two main assumptions. Firstly, surface temperature is computed from satellite data for a particular instant of a typical sunny day. Secondly, due to the topography of the valley there is no consideration of cross–winds. Even though cross–winds are not large in magnitude, (1 to 10 km/h) their presence should be included for a more accurate model. Having said that, there are some possible ways to validate the results.

Scaled models occur in very controlled conditions. The model, which should include topography and temperature of the surface, is difficult to obtain in the laboratory. As well, large–scale effects are difficult to emulate in the laboratory, therefore it is difficult to assess the use of DNS, RANS, LES or k–epsilon methods to properly model buoyancy effects.

Comparison of smoke patterns formed by large chimneys can be done and wind speed can also be sampled at different heights. This comparison can only be possible in small regions. Temperature conditions of the surface need to be available from the Landsat image at the time. The direction and orientation of the smoke produced by chimney stacks could be measured by terrestrial photogrammetric techniques as described in the early work of Orvill 1960 [26] and more recently in Rasmussen et al (2002) [25], coupled with Doppler

radar measurements [27] to obtain speed profiles one could try to correlate the information produced by the model with the sensor data.

8 Conclusions

Wind simulation is being increasingly studied over the past decades. High Performance Computation (HPC) has made more accurate simulations possible in a reasonable time–frame. There are still some problems to be addressed such as the lack of highly accurate terrain models, mesh generation, automatic processing, and also accurate solvers that include all the physical phenomenon relevant to a wind simulation scenario.

The availability of digital elevation models DEM from the Shuttle Radar Topography Mission allows accurate and automatic composition of CFD domains for wind simulations. The scheme proposed here uses a tetrahedral mesh that in spite of its automatic advantages is not optimum when using the Finite Volume Method. Further research needs to be done in the direction of automatic hexahedral generators for complex topographic terrain.

Assessment of the temperature of the terrain is accomplished through band 6 of Landsat 7, which is recognised as the temperature band. This computations rely on the emissivity extracted from bands 3 and 4, producing an accurate map over the region. Emissivities values are function of the terrain material in this simulation. All the NDVI indexes interpolated lie inside the valid boundaries presented on section 5.2. This allows computation of the emissivity based on Lansat information. For future works with different terrain, more research related to the type of vegetation and their emissivity properties should be performed in case the NDVI values are outside range.

The simulation accomplished is made under the assumption than no cross wind exist. The only local source of wind is the natural convection due to surface heating. It is observed the formation of Bénard cells patterns which are convection cells that appear spontaneously in a fluid when heat is applied from below. Although this is a possible scenario for the Aburra Valley, more complex cross wind effects should be considered.

The turbulence model used in this simulation was the k–epsilon model which is not entirely designed to simulate flow at large scales as the present investigation. Future work includes the use of Large Eddy Simulations (LES)

or any other Lagrangian Method to accurately predict the wind's behaviour over the valley. A direct application of this model is the simulation of transport of particles or gas due to pollution.

References

[1] A. Walton, A.Y.S. Cheng and W.C. Yeung. Large–eddy simulation of pollution dispersion in an urban street canyon–part i: comparison with field data. *Atmospheric Environment*, ISSN 1352–2310, **36**(22), 3601–3613 (2002). Referenced in 67

[2] Paolo Monti and Giovanni Leuzzi. A numerical study of mesoscale airflow and dispersion over coastal complex terrain. *International Journal of Environment and Pollution*, ISSN 0957–4352, **25**(1-4), 239–250 (2005). Referenced in 67

[3] Paul Dawson, David E. Stock and Brian Lamb. The numerical simulation of airflow and dispersion in three-dimensional atmospheric recirculation zones. *Journal of applied meteorology*, ISSN 0894–8763, **30**(7), 1005–1024 (1991). Referenced in 67

[4] Si–Wan Kim, Chin–Hoh Moeng, Jeffrey C. Weil, and Mary C. Barth. Lagrangian particle dispersion modeling of the fumigation process using large–eddy simulation. *Journal of athmosferic Sciences*, ISSN 0022–4928, **62**(6), 1932–1946 (2005). Referenced in 67

[5] P. W. Cleary and M. Prakash. Discrete element modelling and smooth particle hydrodynamics: potential in the environmental sciences. *Phil. Transaction of Royal Society*, 362, 2003–2030 (2004). Referenced in 67

[6] Xiuling Wang, Darrell Pepper, Yitung Chen and Sean Hsieh. A three dimensional finite element model for emergency response. *43rd AIAA Aerospace Sciences Meeting and Exhibit*, Reno, Nevada, 2005. Referenced in 67

[7] L. B. Hansen, N. Kamstrup and B. Ulf Hansen. *Estimation of net short-wave radiation by the use of remote sensing and a digital elevation model: a case study of a high arctic mountainous area.* International Journal of Remote Sensing, ISSN 0143–1161, **23**(21), 4699–4718 (2002). Referenced in 67

[8] NGA and NASA. *Shuttle radar topography mission (srtm).* `http://www2.jpl.nasa.gov/srtm/`, 2000. Referenced in 68

[9] Pat L. Scaramuzza, Brian L. Markham, Julia A. Barsi, and Ed Kaita. Landsat–7 etm+ on–orbit reflective–band radiometric characterization. *IEEE Transactions on geoscience and remote sensing*, ISSN 0196–2892, **42**(12), 2796–2809, (December 2004). Referenced in 69

[10] Landsat Project Science Office. *Landsat 7 Science Data Users Handbook*. Goddard Space Flight Center, NASA, Washinghton, 2002. Referenced in 69, 74

[11] P. Dash, F. M. Gottsche, F. S. Olesen and H. Fischer. Land surface temperature and emissivity estimation from passive sensor data: theory and practice–current trends. *International Journal of Remote Sensing*, ISSN 0143–1161, **23**(13), 2563–2594 (2002). Referenced in 69, 73

[12] A. J. Prata, V. C. Coll, J. A Sobrino, and C. Ottle. Thermal remote sensing of land surface temperature from satellites: Current status and future prospects. *Remote Sensing Reviews*, ISSN 0275–7257, 12, 175–224 (1995). Referenced in 70

[13] G. B. Franca and A. P. Cracknell. Retrieval of land and sea surface temperature using noaa-11 avhrr data in north-eastern brazil. *International Journal of Remote Sensing*, **15**(8), 1695–1712 (1994). Referenced in 70

[14] M. A. Friedl. Forward and inverse modeling of land surface energy balance using surface temperature measurements. *Remote Sensing of Environment*, ISSN 0034-4257, **79**(2–3), 344–354 (2002). Referenced in 70

[15] Manuel J. García. *Fixed Grid Finite Element Analysis in Structural Design and Optimization*. PhD Thesis, The University of Sydney, Sydney, 1999. Referenced in 71

[16] Joachim Schöberl. *NETGEN*, 4.3 edition, `http://www.hpfem.jku.at/netgen`. Johannes Kepler University Linz, Austria, 2005. Referenced in 72

[17] T. Schmugge, S. J. Hook, and C. Coll. Recovering surface temperature and emissivity from thermal infrared multispectral data. *Remote Sensing of Environment*, ISSN 0034–4257, **65**(2), 121–131 (1998). Referenced in 73

[18] D.A. Artis and W. H. Carnahan. Survey of emissivity variability in thermography of urban areas. *Remote Sensing of Environment*, ISSN 0034–4257, 12, 313–329 (1982). Referenced in 74

[19] A. Van de Griend and M. Owe. On the relationship between thermal emissivity and the normalized difference vegetation index for natural surfaces. *International Journal of Remote Sensing*, ISSN 0143–1161, **14**(6), 1119–1131 (1993). Referenced in 75

[20] Jinqu Zhang, Yupeng Wang and Yan Li. A C++ program for retrieving land surface temperature from the data of landsat tm/etm+ band6. *Computers & Geosciences*, ISSN 0098–3004, **32**(10), 1796–1805 (2006). Referenced in 75

[21] Michael F. Jansinski. Sensitivity of the normalized difference vegetation index to subpixel canopy cover, soil albedo, and pixel scale. *Remote Sensing of Environment*, ISSN 0034-4257, 32, 169–187 (1990). Referenced in 75

[22] National Oceanic and Atmospheric administration and NASA and United States Airforce. *U.S. Standard atmoshpere*, 1976. Referenced in 77

[23] H.G. Weller, G. Tabor, H. Jasak and C. Fureby. A tensorial approach to computational continuum mechanics using object orientated techniques. *Computers in Physics*, **12**(6), 620–631 (1998). Referenced in 77

[24] Hrvoje Jasak, Henry G. Weller and Niklas Nordin. In-cylinder CFD simulation using a C++ object-oriented toolkit. SAE technical papers, document number 2004-01-0110, 2004. Referenced in 77

[25] Erik N. Rasmussen, Robert Davies-Jones and Ronald L. Holle. Terrestrial photogrammetry of weather images acquired in uncontrolled circumstances. *Journal of atmospheric and oceanic technology*, ISSN 0739–0572, **20**(12), 1790–1803 (2003). Referenced in 80

[26] Harold D. Orvill and A. Richard Kassander Jr. *Terrestrial Photogrammetry of Clouds*. Journal of the Atmospheric Sciences, ISSN 0022–4928, **18**(5), 682–687 (1961). Referenced in 80

[27] R. M. Hardesty, R. M. Banta, M. J. Post and W. L. Eberhard. A decade of atmospheric studies using a pulsed CO_2 Doppler lidar. *Geoscience and Remote Sensing Symposium, 1994. IGARSS '94. Surface and Atmospheric Remote Sensing: Technologies, Data Analysis and Interpretation., International*, IEEE, ISBN 0–7803–1497–2, **2**, 926–928 (1994). Referenced in 81